Research Article

Chemical Potentials of Quarks Extracted from Particle Transverse Momentum Distributions in Heavy Ion Collisions at RHIC Energies

Hong Zhao and Fu-Hu Liu

Institute of Theoretical Physics, Shanxi University, Taiyuan, Shanxi 030006, China

Correspondence should be addressed to Fu-Hu Liu; fuhuliu@163.com

In the framework of a multisource thermal model, the transverse momentum distributions of charged particles produced in nucleus-nucleus (A-A) and deuteron-nucleus (d-A) collisions at relativistic heavy ion collider (RHIC) energies are investigated by a two-component revised Boltzmann distribution. The calculated results are in agreement with the PHENIX experimental data. It is found that the source temperature increases obviously with increase of the particle mass and incident energy, but it does not show an obvious change with the collision centrality. Then, the values of chemical potentials for up, down, and strange quarks can be obtained from the antiparticle to particle yield ratios in a wide transverse momentum range. The relationship between the chemical potentials of quarks and the transverse momentum with different centralities is investigated, too.

1. Introduction

As an interesting research field, high energy heavy ion collisions have a very important significance for understanding of particle physics, nuclear physics, and astrophysics in both theoretical and experimental aspects [1–3]. Investigating the multiparticle production process at high energies provides a unique opportunity for us to comprehend the nuclear reaction mechanism and rare phenomena at high density and high temperature [4–6]. A large number of experimental and theoretical studies have been carried out over an energy range from a few tens of MeV to a few TeV per nucleon in the past decades, and many theoretical models [7–12] have been proposed in the field of multiparticle production to explain the different features of the experimental results, such as angular distributions, multiplicity distributions, transverse momentum (or mass) distributions, (pseudo) rapidity distributions, the longitudinal flow, transverse flow, production cross-sections, and others [13–19].

The relativistic heavy ion collider (RHIC) and the large hadron collider (LHC) [20–22] have been opening new energy regions for the research of multiparticle production

in nuclear collisions. One of the major objectives of them is searching for the evidence of a new state of matter, namely, Quark-Gluon plasma (QGP) [23–26]. Traditionally, QGP is considered crucial to determine whether the thermal and dynamical equilibrations do exist in the interacting region in relativistic collisions [27]. Although this idea was put forward many years ago, up to now there is no unambiguous test to probe the degree of equilibration in the system. For any system, we can get the important thermodynamic information by the chemical potential. The possibility of combining different substances for forming optimal mixtures is strictly related to knowledge of the chemical potential of each component in the mixture environment [28]. In previous literature [27–31], chemical potentials of different particles have been researched with different models and formulas, simple scaling relations connecting chemical potentials are found. However, the study concerning chemical potentials of quarks is correspondingly lacking. In this paper, we will use a practical method to extract chemical potentials of quarks from the antiparticle to particle yield ratios in transverse momentum distributions.

To describe the multifragment emission and multiparticle production processes, we have proposed a multisource thermal model [15–17] and explained some distributions of fragments and particles produced in nuclear collisions in a wider energy range. To give a further test to the multisource thermal model, in this paper, we will describe the transverse momentum distributions of charged particles produced in nucleus-nucleus collisions at RHIC energies by using the model in which the Boltzmann distribution is revised to fit the data at high transverse momentum. Then, the chemical potentials of quarks from the antiparticle to particle yield ratios are extracted in a wide transverse momentum range.

2. The Model

According to the multisource thermal model [15–17] which is used in the descriptions of particle (fragment) multiplicity, emission angles, azimuths, projected angles, (pseudo) rapidity, and transverse flows in high energy collisions, many emission sources are assumed to form in high energy collisions. These sources emit final-state particles and nuclear fragments [18, 18, 32]. Each source is considered to emit particles isotropically in its rest frame and is treated as a thermodynamic system of relativistic and quantum ideal gas [33–36]. We have p_T distribution to be the Boltzmann distribution [18]:

$$f_{p_T}(p_T) = \frac{1}{N}\frac{dN}{dp_T} = Cp_T \exp\left(-\frac{\sqrt{p_T^2 + m_0^2}}{T}\right), \quad (1)$$

where N denotes the number of particles, C is the normalization constant, T is the temperature parameter, and m_0 is the rest mass of the considered particle. Considering multiple temperatures, the p_T distribution can be described by a multicomponent Boltzmann distribution:

$$f_{p_T}(p_T) = \frac{1}{N}\frac{dN}{dp_T} = \sum_{i=1}^{n} k_i C_i p_T \exp\left(-\frac{\sqrt{p_T^2 + m_0^2}}{T_i}\right), \quad (2)$$

where k_i, C_i, and T_i are the contribution ratio, normalization constant, and temperature parameter of the ith source, respectively.

In the case of using the parameters as less as possible, we found that (1) and (2) underestimate the tail part of the transverse momentum distribution. To revise the two equations, we multiply experientially the right side by p_T and make a renormalization. Then, we have a two-component revised Boltzmann distribution to be

$$f_{p_T}(p_T) = \frac{1}{N}\frac{dN}{dp_T} = k_1 C_1 p_T^2 \exp\left(-\frac{\sqrt{p_T^2 + m_0^2}}{T_1}\right)$$
$$+ (1 - k_1) C_2 p_T^2 \exp\left(-\frac{\sqrt{p_T^2 + m_0^2}}{T_2}\right), \quad (3)$$

where k_1 is the contribution ratio of the first temperature, $C_{1,2}$ and $T_{1,2}$ denote the new normalization constant and new

temperature parameter of the first and second components, respectively.

According to the statistical arguments based on chemical and thermal equilibrium at the quark level, we have the relations between antiparticle to particle yield ratios and quark chemical potentials to be [37]

$$\frac{\rho(\overline{p})}{\rho(p)} = \exp\left(-\frac{2(2\mu_u + \mu_d)}{T_p}\right),$$

$$\frac{\rho(\pi^-)}{\rho(\pi^+)} = \exp\left(-\frac{2(\mu_u - \mu_d)}{T_\pi}\right), \quad (4)$$

$$\frac{\rho(K^-)}{\rho(K^+)} = \exp\left(-\frac{2(\mu_u - \mu_s)}{T_K}\right),$$

where ρ is the number density of considered particles; μ_u, μ_d, and μ_s are the chemical potentials of up, down, and strange quarks, respectively; T_p, T_π, and T_K are the temperature parameters extracted from proton (antiproton), negatively (positively) pion, and negatively (positively) kaon spectrums, respectively.

We would like to point out that the chemical potentials of up and down quarks have been differentiated in the above discussions, although the two chemical potentials were not differentiated in previous literature [37]. From (4), the relations between the parameter values and the chemical potentials of quarks can be obtained. Then, the chemical potentials of quarks can be extracted from the antiparticle to particle yield ratios in transverse momentum distributions.

3. Comparisons with Experimental Data

The transverse momentum distributions of π^+/π^-, K^+/K^-, and $p/\overline{p}$ produced in Au-Au collisions at center-of-mass energy per nucleon pair $\sqrt{s_{NN}} = 130$ and $200\,\text{GeV}$ are presented in Figures 1 and 2, respectively. The symbols represent the experimental data with different centralities measured by the PHENIX collaboration [38–40], and the curves are our results calculated by the two-component revised Boltzmann distribution. In the calculation, the values of the fitted parameters are obtained by fitting the experimental data and shown in Table 1 with values of χ^2/dof (χ^2 per degree of freedom). It seems that in most cases the model describes the experimental data. From the parameter values, one can see that the temperature parameter increases with increase of particle mass for emissions of the six types of particles. For emission of π^+/π^-, the temperature does depend nonobviously on impact centrality, and for emission of K^+/K^- and $p/\overline{p}$, the temperature parameter increases with increases of impact centrality.

Figure 3 presents the transverse momentum distributions of positively and negatively charged particles produced in Au-Au and d-Au collisions at $\sqrt{s_{NN}} = 200\,\text{GeV}$ with different centrality classes and magnifications. The symbols represent the experimental data measured by the PHENIX collaboration [41], and the curves are our results calculated by the two-component revised Boltzmann distribution. The fitted parameter values and the corresponding χ^2/dof are given in

TABLE 1: Parameter values corresponding to the curves in Figures 1 and 2 for Au-Au collisions at $\sqrt{s_{NN}}$ = 130 and 200 GeV, respectively. The values for positively/negatively charged particles are given in terms of "the first value/the second value" in the case of the two values being different. The relative errors estimated for $T_{1,2}$ and k_1 are less than 6% and 0.5%, respectively.

Figure	Centrality	Particle	T_1 (GeV)	k_1	T_2 (GeV)	χ^2/dof
Figures 1(a) and 1(b)	0–5%	π^+/π^-	0.091/0.089	0.979/0.982	0.220/0.233	1.412/1.512
		K^+/K^-	0.150/0.110	0.996	0.350/0.300	1.609/1.309
		$p/\bar{p}$	0.192/0.205	0.995/0.979	0.370/0.345	1.461/1.694
Figures 1(c) and 1(d)	15–30%	π^+/π^-	0.087/0.089	0.986/0.985	0.228/0.232	1.575/1.494
		K^+/K^-	0.141/0.130	0.979/0.977	0.260/0.263	1.330/1.042
		$p/\bar{p}$	0.183/0.180	0.989/0.983	0.330/0.304	0.846/1.944
Figures 1(e) and 1(f)	60–92%	π^+/π^-	0.082/0.078	0.995/0.989	0.250/0.215	0.965/0.435
		K^+/K^-	0.075/0.079	0.999	0.230/0.221	1.200/0.905
		$p/\bar{p}$	0.120/0.110	0.999	0.305/0.390	0.931/1.676
Figures 2(a) and 2(b)	0–5%	π^+/π^-	0.122/0.123	0.970/0.969	0.254	0.562/0.634
		K^+/K^-	0.175	0.981/0.979	0.350	0.769/1.245
		$p/\bar{p}$	0.263	0.995/0.993	0.470/0.450	0.281/0.604
Figures 2(c) and 2(d)	60–92%	π^+/π^-	0.114	0.989	0.276	1.879[a]/1.839[a]
		K^+/K^-	0.147	0.993	0.350/0.340	0.413/0.603
		$p/\bar{p}$	0.194/0.190	0.998/0.997	0.430/0.380	0.651/0.542

[a]The last point is not included in the calculation of χ^2/dof due to the low statistics.

TABLE 2: Parameter values corresponding to the curves in Figure 3 for Au-Au and d-Au collisions at $\sqrt{s_{NN}}$ = 200 GeV. The values for positively/negatively charged particles are given in terms of "the first value/the second value" in the case of the two values being different. The relative errors estimated for $T_{1,2}$ and k_1 are less than 6% and 0.5%, respectively.

| Figure	Collision	Particle	Centrality	T_1 (GeV)	k_1	T_2 (GeV)	χ^2/dof
Figures 3(a) and 3(d)	Au-Au 200 GeV	π^+/π^-	0–20%	0.150	0.996	0.400	1.657/1.481
			20–40%	0.160	0.996	0.410	1.168/0.967
			0–100%	0.160	0.995	0.400	1.303/1.026
			40–60%	0.160	0.996	0.400	0.791/0.625
			60–88%	0.180	0.995	0.410	0.552/0.637
Figures 3(a) and 3(d)	d-Au 200 GeV	π^+/π^-	0–10%	0.180	0.998	0.420	1.531/1.144
			10–20%	0.180	0.997	0.410	1.425/1.569
			20–40%	0.175	0.996	0.410/0.405	1.478/1.581
			40–60%	0.168	0.997	0.410	1.442/1.331
			60–92%	0.165	0.997	0.415/0.418	1.741/1.935
Figures 3(b) and 3(e)	Au-Au 200 GeV	K^+/K^-	0–20%	0.220	0.995	0.520	0.426/0.521
			20–40%	0.220	0.996	0.520	0.507/0.657
			0–100%	0.200	0.996	0.500	0.559/0.532
			40–60%	0.200	0.996	0.500	0.272/0.221
			60–88%	0.200	0.997	0.500	0.257/0.461
Figures 3(b) and 3(e)	d-Au 200 GeV	K^+/K^-	0–10%	0.230	0.999	0.700/0.680	1.682/1.679
			10–20%	0.230	0.999	0.670	0.759/0.819
			20–40%	0.230	0.999	0.600/0.580	0.428/0.654
			40–60%	0.210	0.999	0.520	0.981/0.731
			60–92%	0.200	0.998	0.520/0.510	0.584/0.509
Figures 3(c) and 3(f)	Au-Au 200 GeV	$p/\bar{p}$	0–20%	0.250	0.999	0.620/0.580	0.529/0.393
			20–40%	0.250	0.999	0.600/0.560	0.345/0.686
			0–100%	0.250	0.999	0.590/0.550	1.243/1.367
			40–60%	0.250	0.999	0.590/0.550	0.755/1.127
			60–88%	0.230	0.999	0.550/0.500	0.561/0.598
Figures 3(c) and 3(f)	d-Au 200 GeV	$p/\bar{p}$	0–10%	0.282	0.999	0.730/0.700	0.437/0.489
			10–20%	0.282	0.999	0.730/0.680	0.366/0.419
			20–40%	0.282	0.999	0.730/0.680	0.960/0.418
			40–60%	0.260/0.250	0.999	0.710/0.646	1.022/0.901
			60–92%	0.240/0.230	0.999	0.680/0.600	1.274/1.162
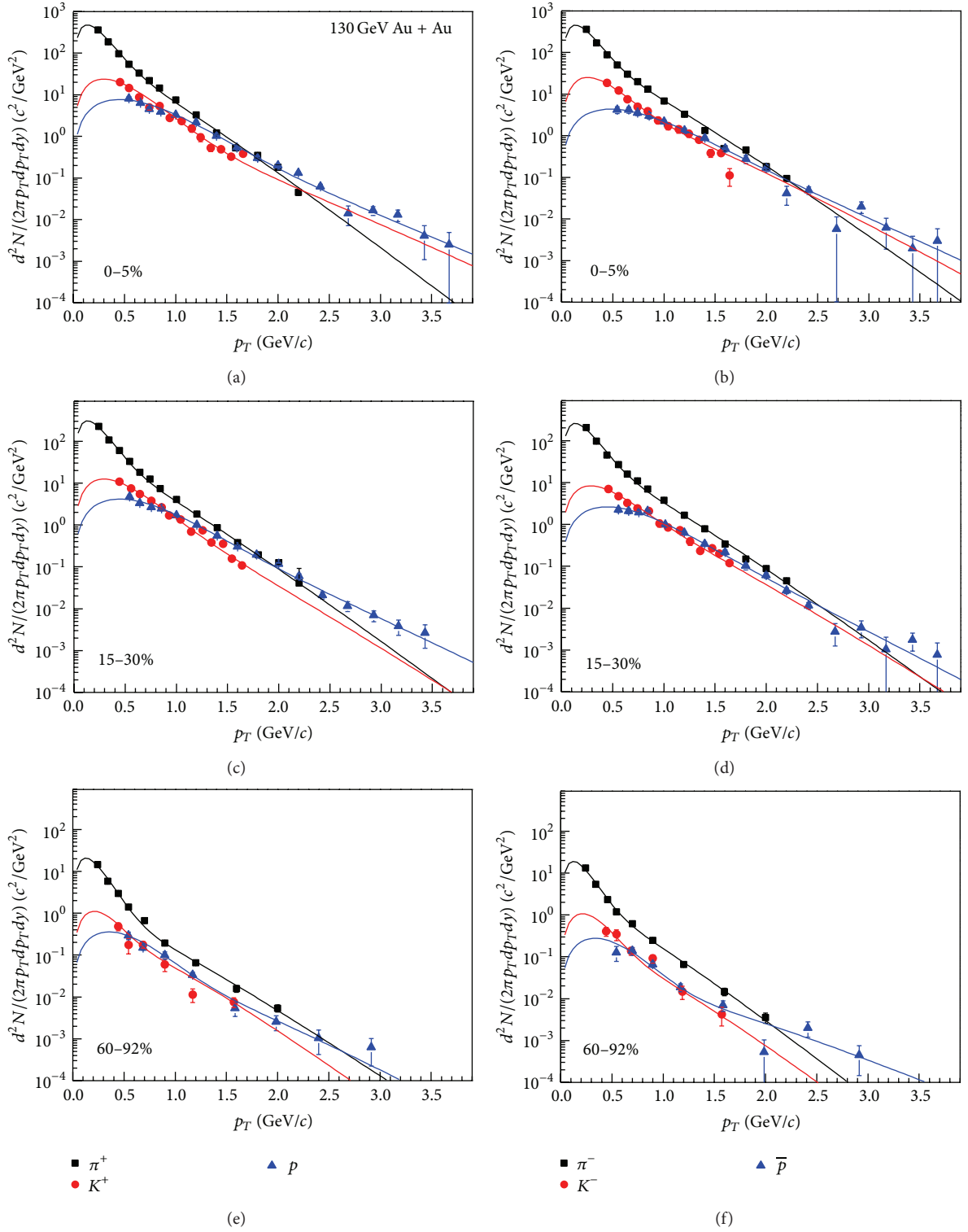
Figure 1: The transverse momentum distributions of π^+/π^-, K^+/K^-, and $p/\overline{p}$ produced in Au-Au collisions at $\sqrt{s_{NN}} = 130$ GeV with different centrality classes. The symbols represent the experimental data of the PHENIX collaboration [38, 39], and the curves are our results calculated by the two-component revised Boltzmann distributions.

TABLE 3: The same as that for Table 2, but showing the results corresponding to the curves in Figure 4 for Au-Au collisions at $\sqrt{s_{NN}}$ = 200 GeV.

Figure	Particle	Centrality	T_1 (GeV)	k_1	T_2 (GeV)	χ^2/dof
Figures 4(a) and 4(b)	π^+/π^-	0–5%	0.128	0.977/0.976	0.265/0.264	0.625/0.686
		5–10%	0.127/0.126	0.978/0.976	0.268/0.265	0.734/1.011
		10–15%	0.124/0.122	0.975/0.976	0.264	0.872/0.846
		15–20%	0.127/0.124	0.983/0.981	0.279/0.276	1.020/1.289
		20–30%	0.128/0.123	0.983/0.984	0.281/0.278	1.349/1.367
		30–40%	0.127/0.126	0.975/0.986	0.291/0.289	0.872/1.622
		40–50%	0.126	0.989/0.987	0.298/0.293	1.953/1.602
		50–60%	0.121/0.120	0.988	0.284	1.833/1.745
		60–70%	0.118	0.991/0.988	0.289/0.281	1.951/1.779[a]
		70–80%	0.116/0.115	0.976/0.992	0.287	1.893/1.746[a]
		80–92%	0.114	0.994	0.290	1.718[b]/1.996[b]
		60–92%	0.122/0.121	0.976/0.989	0.287/0.286	1.757/1.096[a]
Figures 4(c) and 4(d)	K^+/K^-	0–5%	0.190/0.186	0.999/0.998	0.740/0.600	0.666/0.689
		5–10%	0.184/0.182	0.999/0.998	0.740/0.600	1.357/1.129
		10–15%	0.187	0.999	0.740	1.191/1.194
		15–20%	0.187/0.185	0.999	0.740/0.730	0.995/1.386
		20–30%	0.187/0.185	0.999	0.740/0.730	1.009/1.635
		30–40%	0.184/0.182	0.999	0.740/0.730	1.263/1.256
		40–50%	0.181/0.180	0.999/0.997	0.740/0.480	0.949/0.770
		50–60%	0.178/0.181	0.999	0.730	1.317/0.939
		60–70%	0.174	0.999	0.740	1.164/0.729
		70–80%	0.161/0.164	0.999	0.800/0.780	1.462/1.643
		80–92%	0.163	0.999	0.780/0.760	1.142/1.585
		60–92%	0.163/0.164	0.999	0.760/0.720	1.209/1.090
Figures 4(e) and 4(f)	$p/\overline{p}$	0–5%	0.280	0.999	0.800/0.730	0.362/0.332
		5–10%	0.280	0.999	0.720/0.770	0.438/0.892
		10–15%	0.280	0.999	0.730	0.854/0.437
		15–20%	0.276/0.275	0.999	0.730	0.857/1.329
		20–30%	0.278	0.999	0.730/0.740	1.076/1.634
		30–40%	0.254/0.256	0.999	0.610/0.650	0.884/1.174
		40–50%	0.256	0.999	0.730/0.660	1.873/1.268
		50–60%	0.230/0.227	0.999/0.998	0.520/0.465	1.040/0.810
		60–70%	0.214/0.205	0.999	0.570/0.450	1.362/0.819
		70–80%	0.193	0.999	0.490/0.420	0.632/1.371
		80–92%	0.175/0.174	0.999/0.998	0.410/0.380	1.531/1.359
		60–92%	0.197/0.195	0.999/0.998	0.435/0.400	0.854/1.363

[a]The last point is not included in the calculation of χ^2/dof due to the low statistics.
[b]The last two points are not included in the calculation of χ^2/dof due to the low statistics.

Table 2. In the calculation of χ^2/dof, we take the errors to be a half of the symbol size due to that for some data the errors are not available. One can see that our calculated results are in good agreement with the experimental data. From Table 2 we see clearly that for emissions of π^+, K^+, and p (Figures 3(a), 3(b), and 3(c)), as well as π^-, K^-, and $\overline{p}$ (Figures 3(d), 3(e), and 3(f)), the temperature parameter increases with increase of particle mass. For emissions of charged particles, the values of temperature parameters do not change obviously with centrality class, and for each particle in different centrality classes, the temperature parameter closes to a certain value.

The transverse momentum distributions of identified charged particles produced in Au-Au collisions at $\sqrt{s_{NN}}$ = 200 GeV with different centrality classes and magnifications are shown in Figure 4. The symbols represent the experimental data of the PHENIX collaboration [40] and the curves are our results calculated by the two-component revised Boltzmann distribution. We see again that the model describes well the experimental data. Correspondingly, the values of parameters and χ^2/dof are given in Table 3. Once more, for emissions of charged hadrons, the temperature parameter increases with increase of particle mass. In particular, for emissions of $p/\overline{p}$, the temperature parameter increases with increase of impact centrality.

Based on the above successful descriptions on the transverse momentum distributions of particles and antiparticles,

TABLE 4: Mean values ($\overline{\mu}_u$, $\overline{\mu}_d$, and $\overline{\mu}_s$) of chemical potentials obtained from the curves in Figures 5–8, where the errors are the standard deviations.

Figure	Collision	Centrality	$\overline{\mu}_u$ (MeV)	$\overline{\mu}_d$ (MeV)	$\overline{\mu}_s$ (MeV)
		0–5%	5.030 ± 0.459	20.368 ± 0.341	3.087 ± 0.849
Figure 5	Au-Au 130 GeV	15–30%	18.892 ± 0.192	17.586 ± 0.363	13.784 ± 0.950
		60–92%	5.450 ± 0.163	-17.221 ± 1.337	-18.994 ± 0.719
Figure 6	Au-Au 200 GeV	0–5%	14.932 ± 0.097	14.477 ± 0.097	13.722 ± 0.142
		60–92%	15.697 ± 0.345	15.457 ± 0.354	0.886 ± 0.210
		0–10%	17.937 ± 0.048	17.937 ± 0.048	6.739 ± 0.477
		10–20%	20.402 ± 0.252	20.402 ± 0.252	20.402 ± 0.252
Figures 7(a), 7(c), and 7(e)	d-Au 200 GeV	20–40%	19.182 ± 0.384	11.907 ± 0.202	3.136 ± 0.244
		40–60%	19.906 ± 0.122	19.906 ± 0.122	19.906 ± 0.122
		60–92%	16.036 ± 0.213	27.792 ± 0.464	6.042 ± 0.154
		0–20%	18.902 ± 0.149	18.902 ± 0.149	18.902 ± 0.149
Figures 7(b), 7(d), and 7(f)	Au-Au 200 GeV	20–40%	17.093 ± 0.249	17.093 ± 0.249	17.093 ± 0.249
		40–60%	19.999 ± 0.192	19.999 ± 0.192	19.999 ± 0.192
		60–88%	25.587 ± 0.311	25.587 ± 0.311	25.587 ± 0.311
		0–5%	17.269 ± 0.261	17.038 ± 0.222	7.787 ± 0.149
		5–10%	17.001 ± 0.348	14.909 ± 0.226	6.322 ± 0.169
Figures 8(a), 8(c), and 8(e)	Au-Au 200 GeV	10–15%	16.040 ± 0.055	15.698 ± 0.069	9.758 ± 0.176
		15–20%	16.424 ± 0.289	15.966 ± 0.232	6.372 ± 0.097
		20–30%	19.166 ± 0.407	15.268 ± 0.299	9.739 ± 0.176
		30–40%	20.388 ± 0.219	17.859 ± 0.148	11.093 ± 0.091
		40–50%	19.460 ± 0.298	13.982 ± 0.138	5.587 ± 0.612
		50–60%	16.314 ± 0.326	15.870 ± 0.344	4.979 ± 0.361
Figures 8(b), 8(d), and 8(f)	Au-Au 200 GeV	60–70%	17.848 ± 0.427	12.795 ± 0.215	6.112 ± 0.261
		70–80%	14.630 ± 0.356	13.013 ± 0.370	8.727 ± 0.244
		80–92%	3.949 ± 0.187	3.538 ± 0.165	3.869 ± 0.399
		60–92%	16.221 ± 0.258	16.195 ± 0.251	5.557 ± 0.248

we can use (4) to study the chemical potentials of quarks. Figures 5 and 6 present the dependencies of the chemical potentials of (a) up, (b) down, and (c) strange quarks on the transverse momentum in Au-Au collisions at $\sqrt{s_{NN}}$ = 130 and 200 GeV with different centrality classes, respectively. The curves are our results calculated by (4). The mean values (including their standard deviations) of μ_u, μ_d, and μ_s are given in Table 4. We see that μ_u, μ_d, and μ_s do not obviously depend on transverse momentum range and impact centrality.

The relations between the chemical potentials of quarks and the transverse momentum in d-Au and Au-Au collisions at $\sqrt{s_{NN}}$ = 200 GeV with different centralities are presented in Figure 7. The curves are our results calculated by (4). The mean values of μ_u, μ_d, and μ_s are given in Table 4. In some cases the general trend of curves is that μ_u (μ_d) increases with increase of transverse momentum and μ_s decreases with increase of transverse momentum. However, it is hard to say that there is a difference in depending on the transverse momentum, because these differences are in fact statistical fluctuations in the calculation. One can see that μ_u, μ_d, and μ_s do depend nonobviously on impact centrality.

Figure 8 shows the correlations between μ (μ_u, μ_d, and μ_s) and p_T in Au-Au collisions at $\sqrt{s_{NN}}$ = 200 GeV with different centrality classes. The curves are our results obtained by (4). The mean values of different μ are shown in Table 4. Once more, all μ do depend nonobviously on transverse momentum range and impact centrality. The estimated mean values of μ_u, μ_d, and μ_s from the fittings are 16.6 ± 0.3, 15.7 ± 0.3, and 9.6 ± 0.3 MeV, respectively. We see that the difference between μ_u and μ_d is indeed small.

4. Discussions and Conclusions

In the above calculations, we have used the two-component revised Boltzmann distribution in which $p_T^2 \exp(-\sqrt{p_T^2 + m_0^2}/T)$ is used to replace $p_T \exp(-\sqrt{p_T^2 + m_0^2}/T)$ in the original Boltzmann distribution. This revision can give a better description on the tail part of the transverse momentum distribution, while the original one underestimates particle production at high transverse momentum. To reproduce a high probability for particles with high transverse momentum, another revision which uses $p_T \sqrt{p_T^2 + m_0^2} \exp(-\sqrt{p_T^2 + m_0^2}/T)$ instead of $p_T \exp(-\sqrt{p_T^2 + m_0^2}/T)$ was proposed some years ago [42]. In the two revisions, the normalizations have to be reconsidered, respectively.
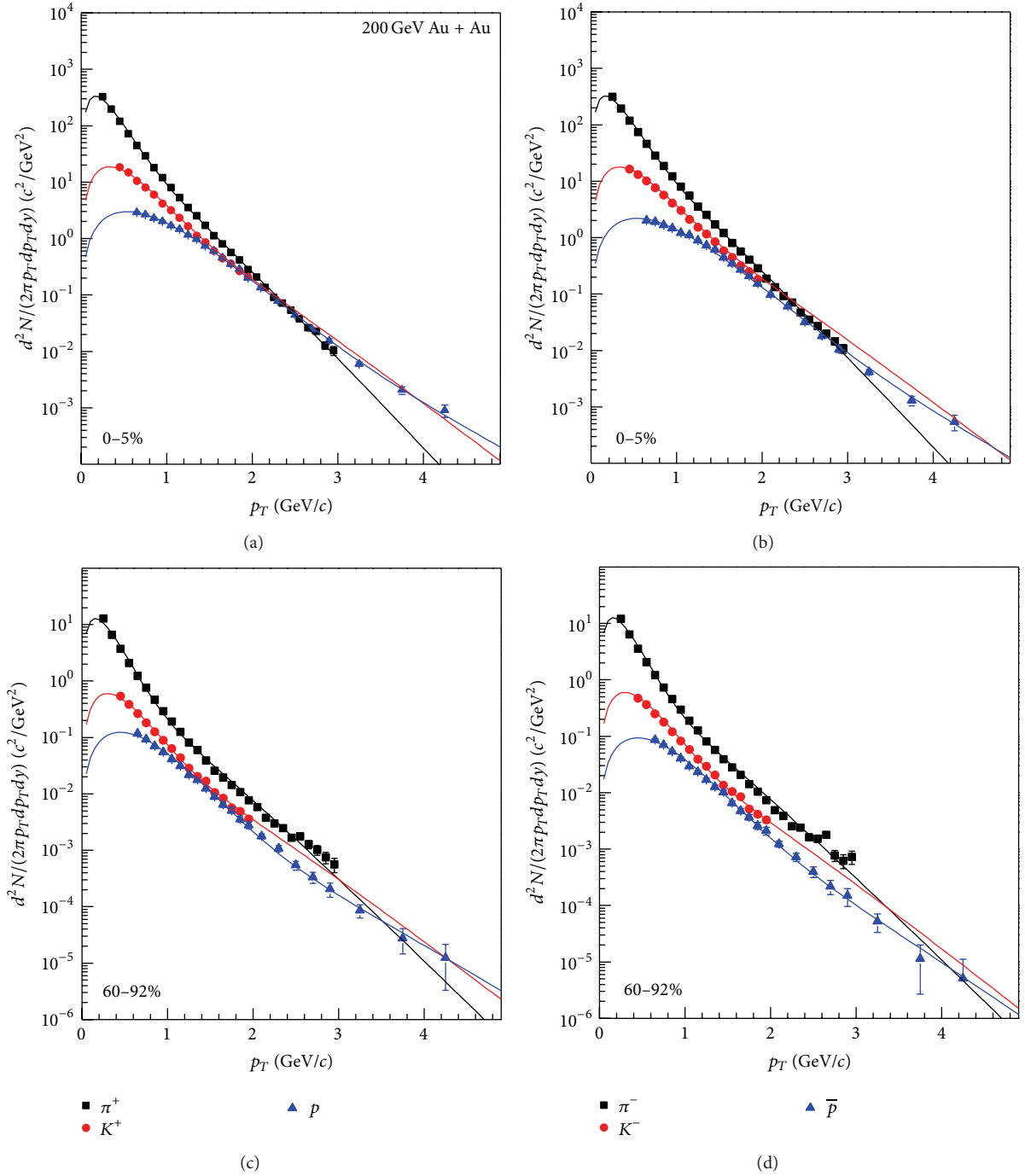
FIGURE 2: The same as Figure 1, but showing the results in Au-Au collisions at $\sqrt{s_{NN}} = 200$ GeV. The symbols represent the experimental data of the PHENIX collaboration [40].

Spectral distributions of final-state particles are very important observations in high energy collisions. Researching the transverse momentum distributions of final-state particles provides a method for us to understand the evolution of interacting systems and the generation mechanism of final-state particles. In previous literature, a number of models and formulas have been used to describe different particles produced in different collisions at different energies. The present work is an approach to give good descriptions

of the transverse momentum distributions with a few free parameters, and chemical potentials of quarks are obtained from the antiparticle and particle yield ratios in a wide transverse momentum range.

The present work is somewhat similar to the previous search [36, 43, 44] but with some different models, parameters, and collisions, where the transverse momentum spectrums of final-state products produced in nucleus-nucleus and proton-proton collisions at high energy have
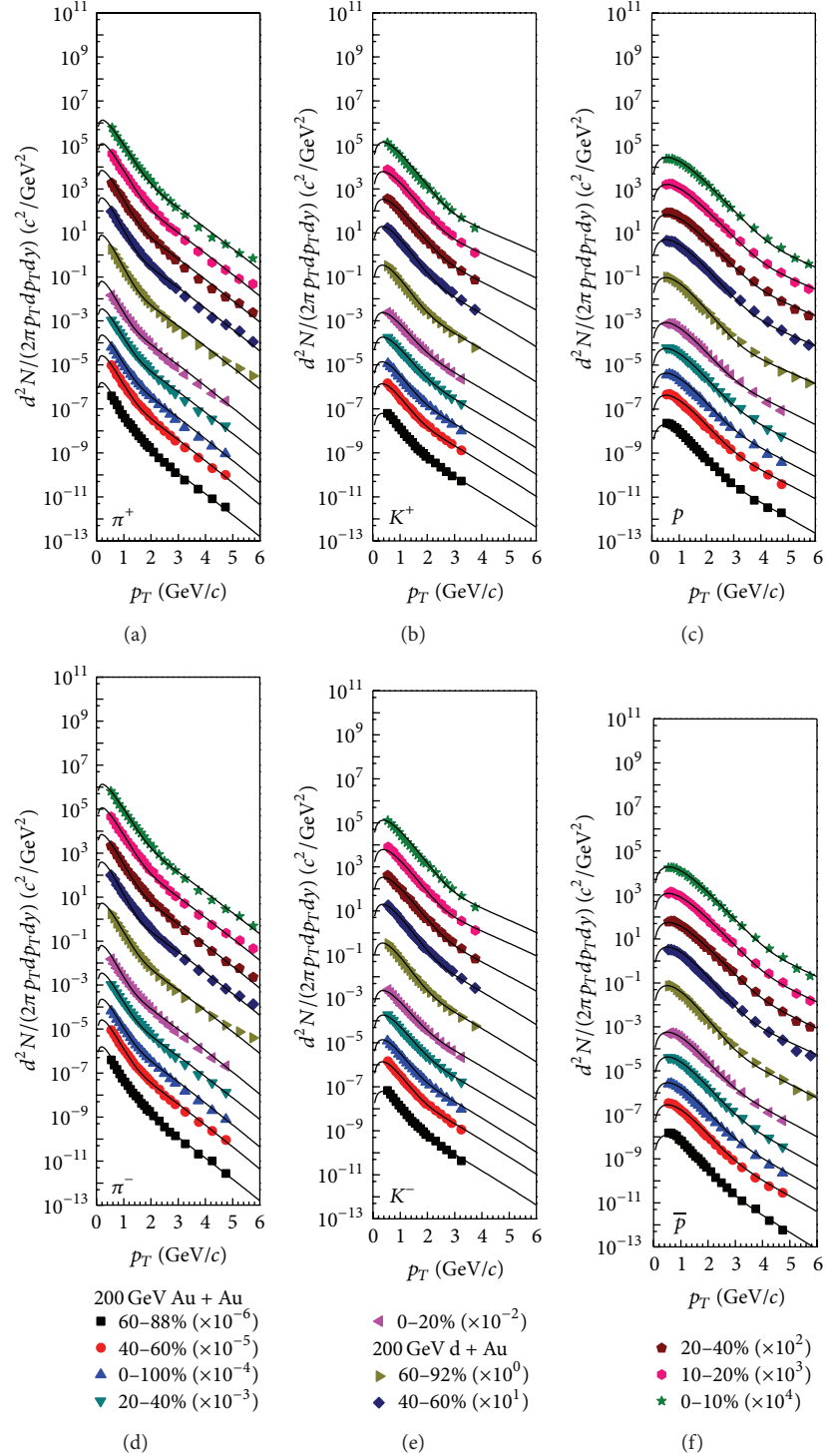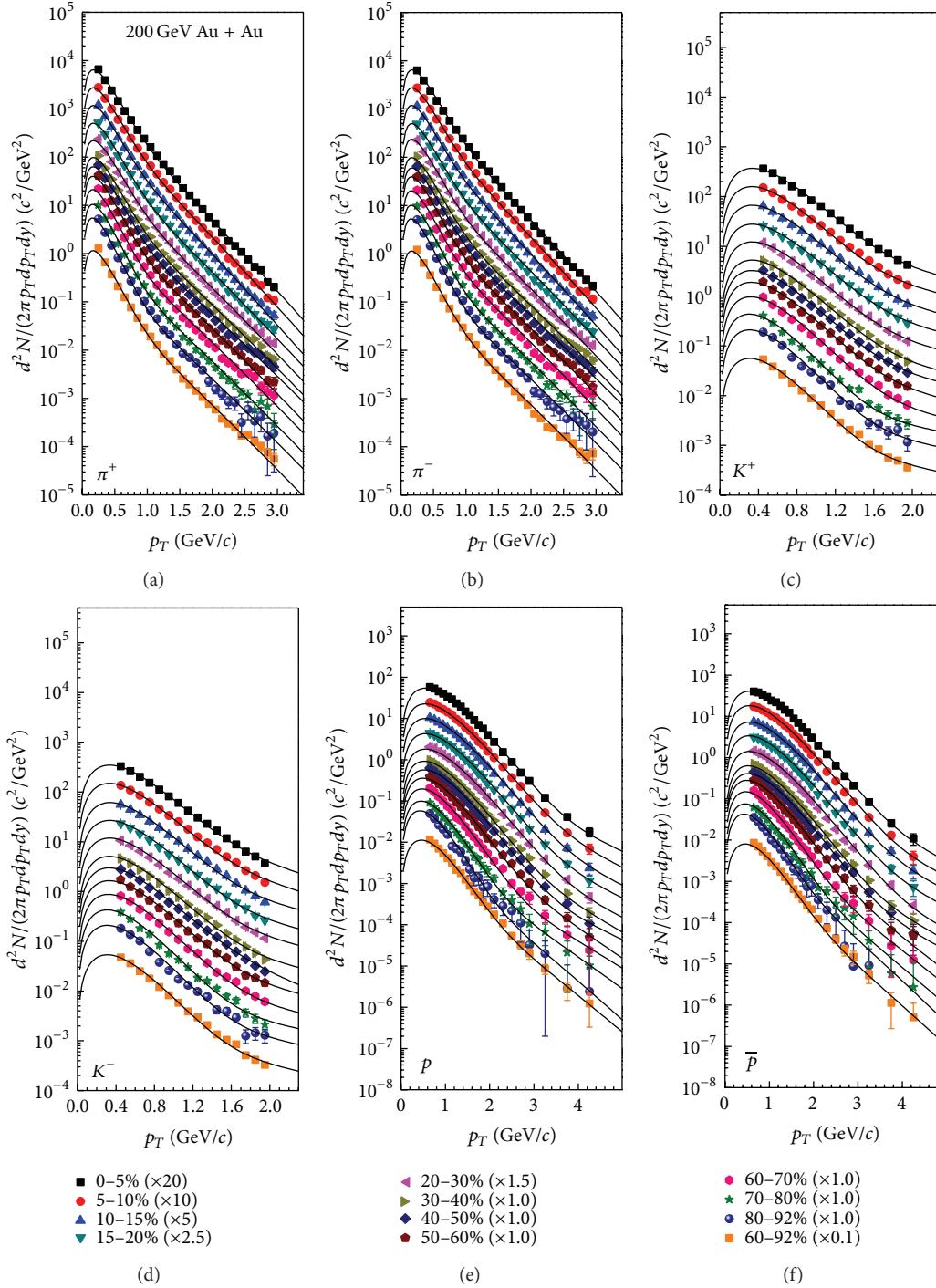
FIGURE 3: The transverse momentum distributions of positively and negatively charged particles in Au-Au and d-Au collisions at $\sqrt{s_{NN}}$ = 200 GeV with different centrality classes and magnifications. The symbols represent the experimental data measured by the PHENIX collaboration [41], and the curves are our results calculated by the two-component revised Boltzmann distributions.

been studied by using the multicomponent Boltzmann distribution, the multicomponent Erlang distribution, and the Lévy distribution. In addition, the present work focuses on the chemical potentials of quarks. We can use different

distributions to describe the same transverse momentum spectrum. Then, the chemical potentials of quarks are extracted from the ratios of negatively/positively charged particles and temperature parameters [45]. Because different

FIGURE 4: The transverse momentum distributions of negatively and positively charged particles produced in Au-Au collisions at $\sqrt{s_{NN}} = 200$ GeV with different centrality classes and magnifications. The symbols represent the experimental data of the PHENIX collaboration [40], and the curves are our results calculated by the two-component revised Boltzmann distributions.

distributions result in different temperatures, we need to correct the temperatures to a standard one when we compare these results.

The present work provides a new variety and professional analysis for collisions that may give a more complete picture of the RHIC and helpful in understanding quark chemical potentials behavior, as well as the relationship between the chemical potentials of quarks and the transverse momentum with a few free parameters and different centralities. Although we have studied the chemical potentials of quarks

(a)

(b)

(c)
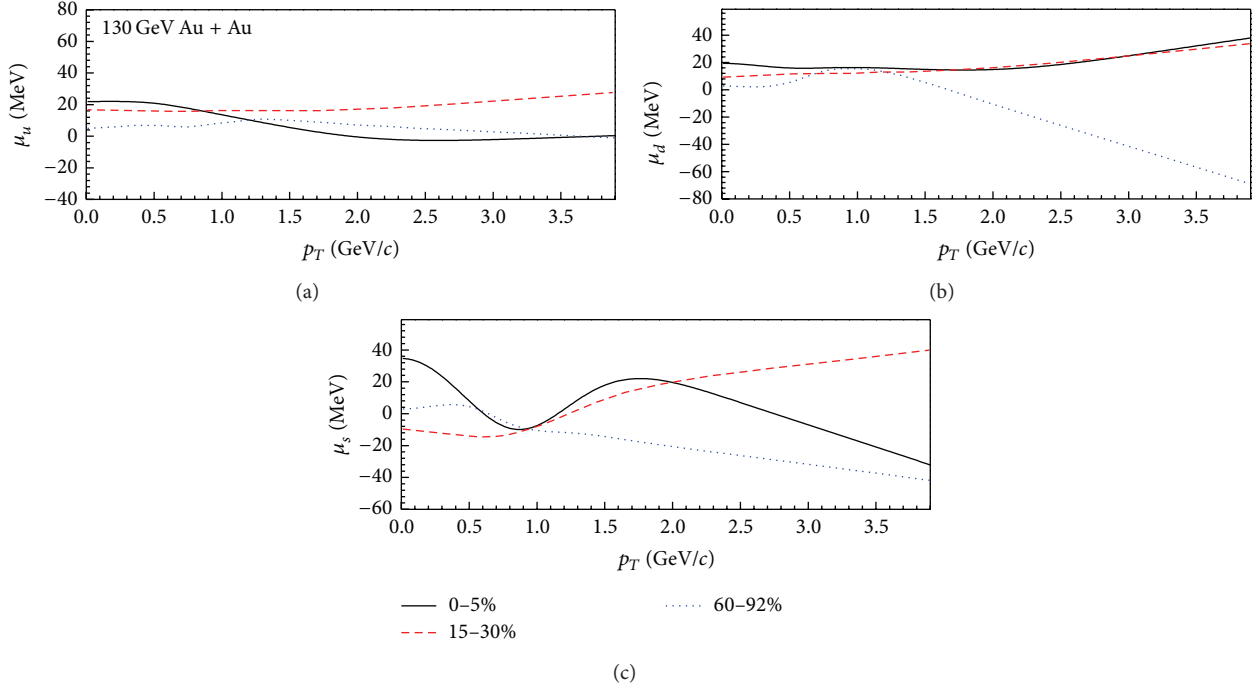
FIGURE 5: Correlations between chemical potentials of quarks and the transverse momentum in Au-Au collisions at $\sqrt{s_{NN}} = 130\,\text{GeV}$ with different centrality classes. The curves are our results calculated by (4).
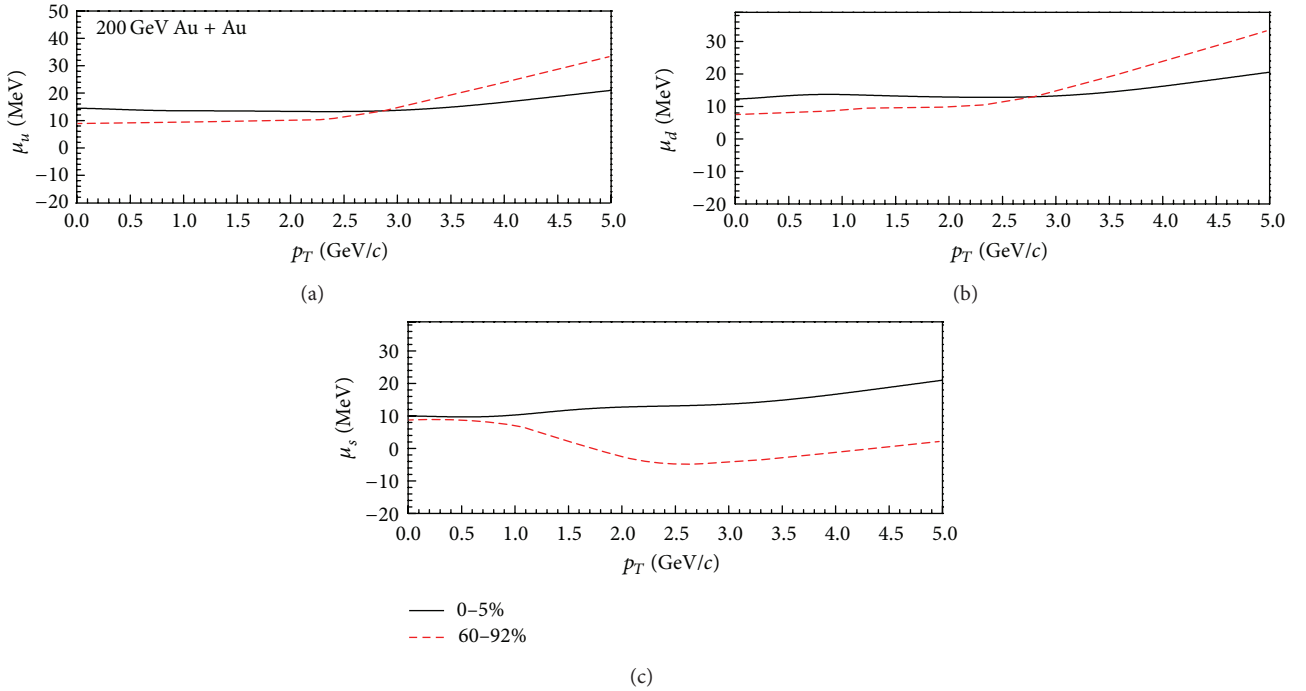

(a)

(b)

(c)

FIGURE 6: The same as Figure 5, but showing the results in Au-Au collisions at $\sqrt{s_{NN}} = 200\,\text{GeV}$.

at different transverse momentums, it does not mean that there is dependence of quark chemical potential on transverse momentum.

In conclusion, the transverse momentum distributions of charged particles produced in Au-Au and d-Au collisions at RHIC energies have been studied by the multisource thermal model. It is shown that the two-component revised Boltzmann distribution is successful in the descriptions of experimental data. For emissions of charged particles, the temperature parameter increases with increases of particle
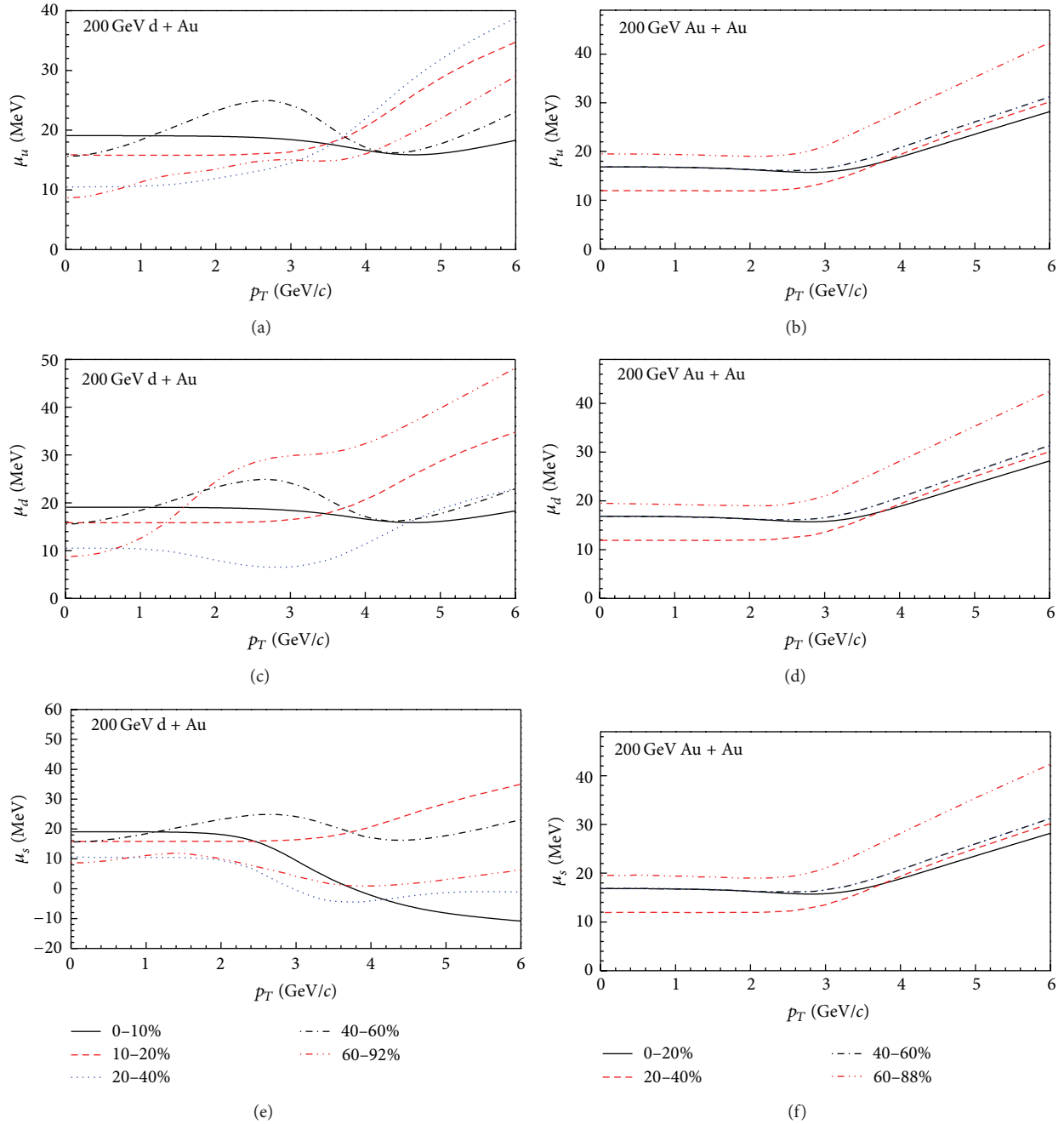
FIGURE 7: Correlations between μ (μ_u, μ_d, and μ_s) and p_T in d-Au and Au-Au collisions at $\sqrt{s_{NN}}$ = 200 GeV with different centrality classes. The curves are our calculated results.

mass and incident energy. In most cases, the temperature parameter does not obviously depend on impact centrality.

In the study of phase transition or thermodynamical and chemical equilibrium, it is quite important to achieve a thorough understanding of the quark chemical potentials. In the present work, we have used a practical method for calculating the quark chemical potentials. The antiparticle to particle yield ratios obtained by the model give the quark chemical potentials in a wide transverse momentum range. We would like to point out that the considered three types

of quark chemical potentials do not show an obvious change with the increase of transverse momentum and impact centrality in nucleus-nucleus collisions at RHIC energies, and in most cases the mean values of μ_u and μ_d are small and the mean values of μ_s are smaller.

The difference between μ_u and μ_d is small due to the small mass difference between up and down quarks. The small values of μ_u, μ_d, and μ_s at RHIC energies indicate that the chemical potentials of other quarks are impossibly large. This renders that the interactions among quarks in the interacting
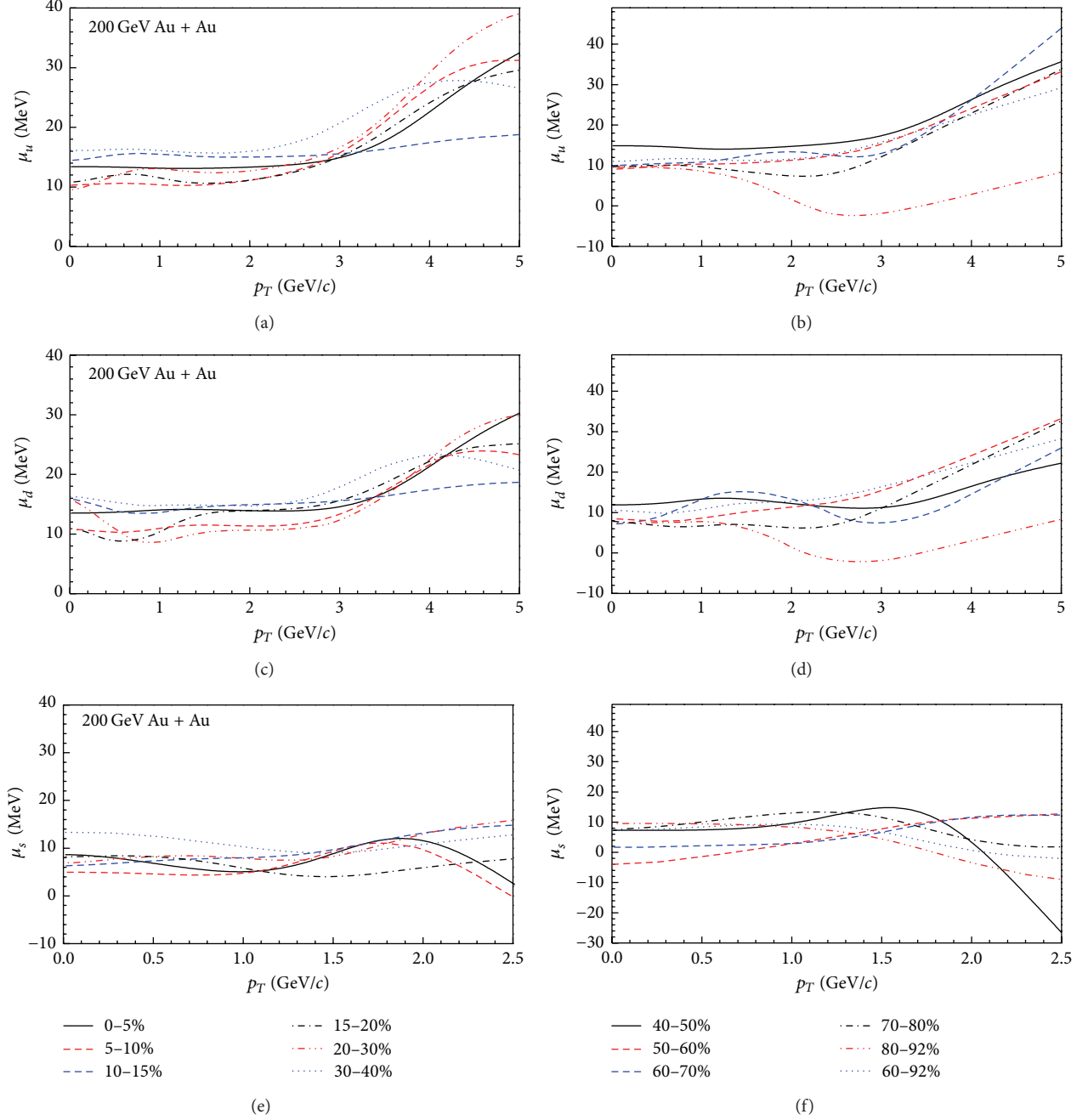
FIGURE 8: The same as Figure 7, but showing only the results in Au-Au collisions at $\sqrt{s_{NN}}$ = 200 GeV for more centrality classes.

system are not too strong, and the interacting system may stay at the state of QGP. The small chemical potentials of quarks result in small chemical potentials of hadrons. According to the general relation between temperature and hadron chemical potential, we have a high temperature of interacting system, which is expected by the formation of QGP.

Conflict of Interests

The authors declare that there is no conflict of interests regarding the publication of this paper.

and the Overseas Training Project for Teachers at Shanxi University.

References

[1] E. L. Bratkovskaya, S. M. Kiselev, and G. B. Sharkov, "Direct photon production from hadronic sources in high-energy heavy-ion collisions," *Physical Review C*, vol. 78, no. 3, Article ID 034905, 10 pages, 2008.

[2] H.-L. Li, F.-M. Liu, G.-L. Ma, X.-N. Wang, and Y. Zhu, "Mach cone induced by γ-triggered jets in high-energy heavy-ion collisions," *Physical Review Letters*, vol. 106, no. 1, Article ID 012301, 4 pages, 2011.

[3] A. Dumitru, E. Molnár, and Y. Nara, "Entropy production in high-energy heavy-ion collisions and the correlation of shear viscosity and thermalization time," *Physical Review C: Nuclear Physics*, vol. 76, no. 2, Article ID 024910, 9 pages, 2007.

[4] M. Murray and BRAHMS Collaboration, "Is there more than one thermal source?" *Journal of Physics G: Nuclear and Particle Physics*, vol. 31, no. 6, pp. S1137–S1140, 2005.

[5] B. B. Back, R. R. Betts, J. Chang et al., "Baryon rapidity loss in relativistic Au+Au collisions," *Physical Review Letters*, vol. 86, no. 10, pp. 1970–1973, 2001.

[6] R. A. Lacey, D. Reynolds, A. Taranenko et al., "Acoustic scaling of anisotropic flow in shape-engineered events: implications for extraction of the specific shear viscosity of the quark gluon plasma," http://arxiv.org/abs/1311.1728v2.

[7] G. D. Westfall, J. Gosset, P. J. Johansen et al., "Nuclear Fireball Model for proton inclusive spectra from relativistic heavy-ion collisions," *Physical Review Letters*, vol. 37, no. 18, pp. 1202–1205, 1976.

[8] G. Burau, J. Bleibel, C. Fuchs, A. Faessler, L. V. Bravina, and E. E. Zabrodin, "Anisotropic flow of charged and identified hadrons in the quark-gluon string model for Au+Au collisions at $\sqrt{s_{NN}}$ = 200 GeV," *Physical Review C*, vol. 71, Article ID 054905, 10 pages, 2005.

[9] X.-N. Wang and M. Gyulassy, "Gluon shadowing and jet quenching in $A + A$ collisions at $\sqrt{s_{NN}}$ = 200 GeV," *Physical Review Letters*, vol. 68, no. 10, pp. 1480–1483, 1992.

[10] B.-A. Li and C. M. Ko, "Formation of superdense hadronic matter in high energy heavy-ion collisions," *Physical Review C*, vol. 52, no. 4, pp. 2037–2063, 1995.

[11] Y. Pang, T. J. Schlagel, and S. H. Kahana, "Cascade for relativistic nucleus collisions," *Physical Review Letters*, vol. 68, no. 18, pp. 2743–2746, 1992.

[12] A. Jahns, C. Spieles, R. Mattiello et al., "Antibaryon shadowing in massive $Au + Au$ collisions at 11 AGeV," *Nuclear Physics A*, vol. 566, pp. 483–486, 1994.

[13] K. Aamodt, B. Abelev, and A. A. Quintana, "(ALICE Collaboration). Elliptic f low of charged particles in Pb-Pb collisions at $\sqrt{s_{NN}}$ = 2.76 TeV," *Physical Review Letters*, vol. 105, Article ID 252302, 11 pages, 2010.

[14] P. Bozek and I. Wyskiel-Piekarska, "Particle spectra in Pb-Pb collisions at $\sqrt{s_{NN}}$ = 2.76 TeV," *Physical Review C: Nuclear Physics*, vol. 85, Article ID 064915, 6 pages, 2012.

[15] F.-H. Liu, "Longitudinal and transverse flows of protons in 2-8 A GeV Au-Au collisions," *Europhysics Letters*, vol. 63, no. 2, pp. 193–199, 2003.

[16] F.-H. Liu, N. N. Abd Allah, D.-H. Zhang, and M.-Y. Duan, "Angular distributions of target black fragments in nucleus-nucleus collisions at high energy," *International Journal of Modern Physics E*, vol. 12, no. 5, pp. 713–723, 2003.

[17] F.-H. Liu, N. N. Abd Allah, and B. K. Singh, "Dependence of black fragment azimuthal and projected angular distributions on polar angle in silicon-emulsion collisions at 4.5A GeV/c," *Physical Review C*, vol. 69, no. 5, Article ID 05760, 4 pages, 2004.

[18] F.-H. Liu, "Unified description of multiplicity distributions of final-state particles produced in collisions at high energies," *Nuclear Physics A*, vol. 810, no. 1–4, pp. 159–172, 2008.

[19] C.-R. Meng, "Transverse momentum and rapidity distributions of ϕ mesons produced in Pb-Pb collisions at SPS energies," *Chinese Physics Letters*, vol. 26, no. 10, Article ID 102501, 4 pages, 2009.

[20] B. B. Back, M. D. Baker, D. S. Barton et al., "Charged-particle pseudorapidity density distributions from Au + Au collisions at $\sqrt{s_{NN}}$ = 130 GeV," *Physical Review Letters*, vol. 87, no. 10, Article ID 102303, 4 pages, 2001.

[21] I. G. Bearden, D. Beavis, C. Besliu et al., "Pseudorapidity distributions of charged particles from Au + Au collisions at the maximum RHIC energy, $\sqrt{s_{NN}}$ = 200 GeV," *Physical Review Letters*, vol. 88, no. 20, Article ID 202301, 4 pages, 2002.

[22] A. Toia, "Bulk properties of Pb-Pb collisions at $(\sqrt{s_{NN}})$ = 2.76 TeV measured by ALICE," *Journal of Physics G*, vol. 38, Article ID 124007, 8 pages, 2011.

[23] J. Rafelski and B. Müller, "Strangeness production in the quark-gluon plasma," *Physical Review Letters*, vol. 48, no. 16, pp. 1066–1069, 1982.

[24] J. Steinheimer and M. Bleicher, "Extraction of the sound velocity from rapidity spectra: evidence for QGP formation at FAIR/RHIC-BES energies," *The European Physical Journal A*, vol. 48, Article ID 100, 5 pages, 2012.

[25] S. Uddin, "Fast hadronization of a quark gluon plasma and meson production," *Physics Letters B*, vol. 406, no. 1-2, pp. 123–129, 1997.

[26] M. Lublinsky and E. Shuryak, "How much entropy is produced in strongly coupled quark-gluon plasma (sQGP) by dissipative effects?" *Physical Review C*, vol. 76, no. 2, Article ID 021901, 4 pages, 2007.

[27] L. A. Stiles and M. Murray, "Limiting fragmentation of chemical potentials in heavy ion collisions," 2006, http://arxiv.org/abs/nucl-ex/0601039.

[28] A. Agarwal, H. Wang, C. Schütte, and L. D. Site, "Chemical potential of liquids and mixtures via adaptive resolution simulation," http://arxiv.org/abs/1311.6982.

[29] A. Z. Mekjian, "Properties of baryonic, electric and strangeness chemical potentials and some of their consequences in relativistic heavy ion collisions," *Physics Letters B*, vol. 651, no. 1, pp. 33–38, 2007.

[30] J. Takahashi, T. Sasaki, and K. Nagata, "Heavy quark potential at finite imaginary chemical potential," in *Proceedings of the 31st International Symposium on Lattice Field Theory (Lattice '13)*, Mainz, Germany, July-August 2013.

[31] A. A. Andrianov, D. Espriu, and X. Planells, "Chemical potentials and parity breaking: the Nambu-Jona-Lasinio model," in *Proceedings of the 31st International Symposium on Lattice Field Theory (Lattice '13)*, Mainz, Germany, July-August 2013.

[32] F.-H. Liu, J.-S. Li, and M.-Y. Duan, "Light fragment emission in ^{86}Kr-^{124}Sn collisions at 25 MeV/nucleon," *Physical Review C: Nuclear Physics*, vol. 75, no. 5, Article ID 054613, 5 pages, 2007.

[33] J. L. Synge, *The Relativistic Gas*, North-Holland, Amsterdam, The Netherlands, 1957.

[34] C. D. Dermer, "The production spectrum of a relativistic Maxwell-Boltzmann gas," *The Astrophysical Journal*, vol. 280, part 1, pp. 328–333, 1984.

[35] F.-H. Liu, C.-X. Tian, M.-Y. Duan, and B.-C. Li, "Relativistic and quantum revisions of the multisource thermal model in high-energy collisions," *Advances in High Energy Physics*, vol. 2012, Article ID 287521, 9 pages, 2012.

[36] F.-H. Liu, Y.-H. Chen, H.-R. Wei, and B.-C. Li, "Transverse momentum distributions of final-state particles produced in soft excitation process in high energy collisions," *Advances in High Energy Physics*, vol. 2013, Article ID 965735, 15 pages, 2013.

[37] I. Arsene, I. G. Bearden, D. Beavis et al., "Quark-gluon plasma and color glass condensate at RHIC? The perspective from the BRAHMS experiment," *Nuclear Physics A*, vol. 757, no. 1-2, pp. 1–27, 2005.

[38] K. Adcox, S. S. Adler, N. N. Ajitanand et al., "Centrality dependence of $\pi^{+/-}$, $K^{+/-}$, p, and $\overline{p}$ production from $\sqrt{s_{NN}}$ = 130 GeV Au+Au collisions at RHIC," *Physical Review Letters*, vol. 88, Article ID 242301, 6 pages, 2002.

[39] K. Adcox, S. S. Adler, N. N. Ajitanand et al., "Single identified hadron spectra from $\sqrt{s_{NN}}$ = 130 GeV Au+Au Collisions," *Physical Review C*, vol. 69, Article ID 024904, 29 pages, 2004.

[40] S. S. Adler, S. Afanasiev, C. Aidala et al., "Identified charged particle spectra and yields in Au+Au collisions at $\sqrt{s_{NN}}$ = 200 GeV," *Physical Review C*, vol. 69, Article ID 034909, 32 pages, 2004.

[41] A. Adare et al., "Spectra and ratios of identified particles in Au+Au and d+Au collisions at $\sqrt{s_{NN}}$ = 200 GeV," *Physical Review C*, vol. 88, Article ID 024906, 16 pages, 2013.

[42] E. Schnedermann, J. Sollfrank, and U. Heinz, "Thermal phenomenology of hadrons from 200A GeV S+S collisions," *Physical Review C*, vol. 48, no. 5, pp. 2462–2475, 1993.

[43] Y.-Q. Gao, C.-X. Tian, M.-Y. Duan, B.-C. Li, and F.-H. Liu, "Transverse momentum distributions of identified particles produced in pp, p(d)A, and AA collisions at high energies," *Pramana—Journal of Physics*, vol. 79, no. 6, pp. 1407–1423, 2012.

[44] H.-R. Wei, Y.-H. Chen, L.-N. Gao, and F.-H. Liu, "Comparing multicomponent Erlang distribution and Lévy distribution of particle transverse momentums," *Advances in High Energy Physics*, vol. 2014, Article ID 782631, 16 pages, 2014.

[45] F.-H. Liu, T. Tian, H. Zhao, and B.-C. Li, "Extracting chemical potentials of quarks from ratios of negatively/positively charged particles in high-energy collisions," *The European Physical Journal A*, vol. 50, article 62, 8 pages, 2014.